Antireflection structure for an effective refractive index near-zero medium in a two-dimensional photonic crystal

Hideo Iizuka[1] and Nader Engheta[2]

[1]*Toyota Central Research and Development Laboratory, Nagakute, Aichi 480 1192, Japan*

[2]*Department of Electrical and Systems Engineering, University of Pennsylvania, Philadelphia, Pennsylvania 19104, USA*

(Received 29 May 2014; revised manuscript received 20 August 2014; published 10 September 2014)

Two-dimensional dielectric photonic crystals (PCs) having periodic air hole cylinders, when designed properly, exhibit near-zero effective refractive index and the wave impedance is dependent on local observation points. The incident wave is mostly reflected at the PC-air interface due to large impedance mismatch. We show, analytically and numerically, that even in the near-zero effective refractive index case the reflection can be suppressed by utilizing an antireflection structure consisting of a PC with the same lattice constant but a different radius for the periodic air hole cylinders. The antireflection PC must be truncated at properly selected cross sections in order to possess the same impedance at cross sections with the host PC and with the air structure. An analytical model combined with the plane-wave expansion method captures the antireflection behavior obtained by the full wave simulations.

DOI: 10.1103/PhysRevB.90.115412 PACS number(s): 42.70.Qs, 42.79.Wc, 42.25.Gy

I. INTRODUCTION

Electromagnetic wave propagation in material media is macroscopically characterized by the permittivity and permeability of the medium. Metamaterials with extreme parameters, particularly, epsilon-near-zero (ENZ) media, have offered unprecedented electromagnetic properties [1]. Those include tunneling of electromagnetic energy through an arbitrarily shaped ultranarrow channel [2–8], electric field levitation [9], transporting an image through a subwavelength hole [10], and boosting nonlinear effects [11]. Moreover, ENZ metamaterials have inspired concepts of nanocircuit boards and elements [12–14] and microwave, optical, and thermal devices [15–19]. Significant experimental works have verified some of the unique features in those frequency ranges [20–27].

Photonic crystals (PCs) allow one to engineer the effective refractive index with a wide range of values, including negative and near-zero values, and therefore exhibit such intriguing properties [28–32]. The wave impedance in PCs is dependent on local observation points [33–35]. Consequently, much effort has been devoted over the past decades to suppress the reflection at the PC-air interface for positive and negative effective refractive indices; gratings [36–38], periodic holes and rods [39–42], gradually changed hole diameters [43], and projected air holes [44] are among the various techniques that have been considered. The development of antireflection for near-zero effective refractive index PCs is challenging method due to large impedance mismatch, and to the best of our knowledge, there has been no report on efficient antireflection structures for such cases of near-zero effective refractive index.

In this paper, we show that even in the near-zero effective refractive index case the reflection can be suppressed by utilizing an antireflection structure consisting of a PC with the same lattice constant but a different radius in the air hole cylinders. Such antireflection PCs have an advantage of adjustable impedance by varying the hole radius. Truncating the antireflection PC at properly selected cross sections enables the same impedance at interfaces with the host PC and with the air structure; therefore, antireflection behavior can be obtained.

This paper is organized as follows. In Sec. II, we present a brief overview of the effective refractive index and the transverse impedance of PCs. We introduce an antireflection structure in Sec. III and validate the effectiveness of the antireflection behavior with numerical results in Sec. IV. The paper is then concluded in Sec. V.

II. EFFECTIVE REFRACTIVE INDEX AND TRANSVERSE IMPEDANCE IN INFINITE PCs

It is important to appreciate the behavior of electromagnetic waves propagating in a near-zero effective refractive index PC in order to consider an antireflection structure. In this section, we briefly review the effective refractive index and the transverse impedance in an infinite two-dimensional PC case.

We consider a typical two-dimensional PC that has the hexagonal arrangement of periodic air hole cylinders with the excitation of the transverse magnetic (TM) wave (electric field is parallel to the air hole cylinders), as shown in Fig. 1(a). The PC has a refractive index of $n_d = 3.48$ for the dielectric material and a lattice constant of $a = 600$ nm for air hole cylinders. The PC exhibits near-zero effective refractive index as a small negative value near the edge of the second band in the dispersion characteristic. The plane-wave expansion method is widely used for the analysis of PCs in which Maxwell's equations are exactly solved by expanding the electromagnetic fields with a plane-wave basis set [45]. Consequently, the vector nature of the electromagnetic fields is fully taken into account. We calculate the equifrequency contours in the two-dimensional wave vectors in the PC of Fig. 1 by using the plane-wave expansion method and then present the results as the angular variation of the effective refractive indices [28] for clear demonstration of the behavior in this article. The angular variation of the effective refractive indices at a design wavelength of $\lambda_{0,a} = 1555.35$ nm is plotted in Fig. 1(b) with variation of the radius of air hole cylinders. We note that small absolute values of effective refractive indices provide an omnidirectional nature, consistent with [28]. Consequently,

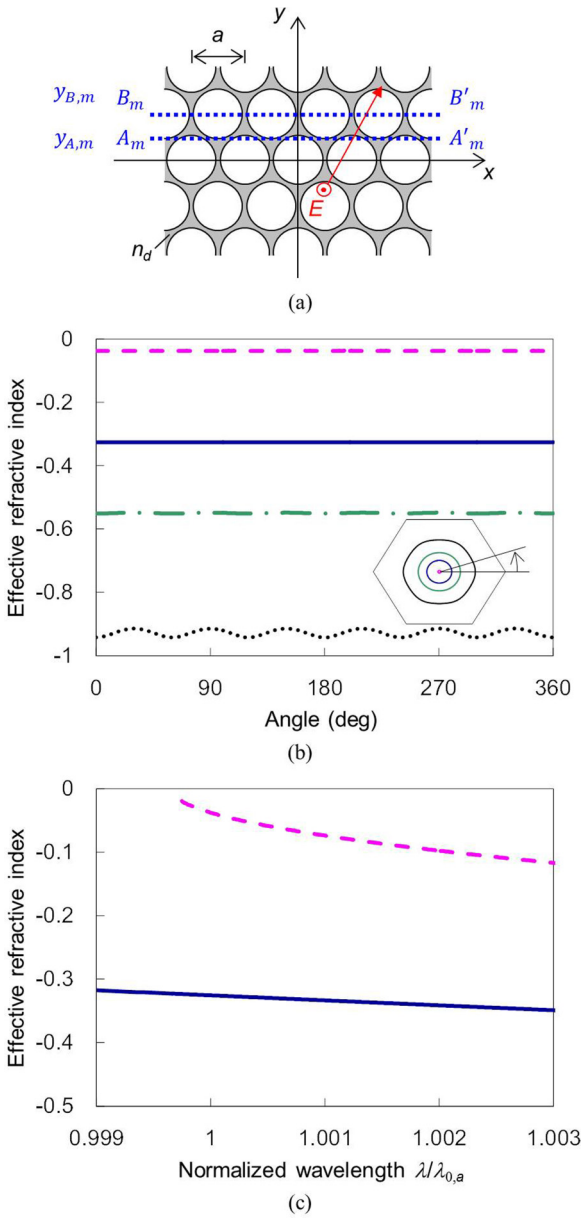

FIG. 1. (Color online) (a) Geometry of a two-dimensional photonic crystal having periodic air hole cylinders ($a = 600$ nm, $n_d = 3.48$). Two cross sections described in Eqs. (2a) and (2b) are indicted by the blue dotted lines. (b) Angular variation of effective refractive indices for different values of the radius of the air cylinders at $\lambda_{0,a} = 1555.35$ nm. The inset shows the equifrequency contours (pink dashed line: 264 nm, blue solid line: 269 nm, green dotted-dashed line: 275 nm; black dotted line: 285 nm). (c) Variation of effective refractive indices as a function of normalized wavelength for radii of $r_h = 264$ mm (pink dashed line) and $r_{ar} = 269$ mm (blue solid line).

we can assume isotropic media in an analytic model as long as we use such small effective refractive indices. The two radii $r_h = 264$ nm (pink dashed line) and $r_{ar} = 269$ nm (blue solid line) of air hole cylinders are used for the host PC and the antireflection PC, respectively. On the other hand, ripples are seen in the angular variation in Fig. 1(b) as the absolute value of the effective refractive index increases.

The variation of the two effective refractive indices as a function of wavelength is shown in Fig. 1(c). The horizontal axis is the normalized wavelength (with respect to the design wavelength $\lambda_{0,a}$ for the analytical results throughout the paper for comparison with numerical results). Small absolute value of the effective refractive index of the host PC (pink dashed line) is more sensitive to the wavelength variation than that of the antireflection PC (blue solid line), since the operation point for the small refractive index is close to the band edge in the dispersion characteristic.

Since the wave impedance is dependent on the local observation points (i.e., local cross section for the observation plane), we must elucidate the impedance behavior quantitatively. The transverse impedance of the cross section parallel with the x-z plane, is defined as the ratio of the averaged electric field to the averaged transverse magnetic field and is given by [34]

$$Z(y) = \frac{\int_{x_0}^{x_0+a} E_z(x,y)\,dx}{\int_{x_0}^{x_0+a} H_x(x,y)\,dx}, \tag{1}$$

where the electric field $E_z(x,y)$ and the magnetic field component $H_x(x,y)$ are calculated using the plane-wave expansion method. The phase velocity of the propagating wave is antiparallel to the group velocity of the power flow in a negative refractive index medium. We consider the power flow in the positive y direction together with the negative sign of the y component of the wave vector. The impedance in Eq. (1) has a positive real part [46]. In addition, the impedance in Eq. (1) has a periodicity of $(\sqrt{3}/2)a$ along the y axis. Thus, we select two typical cross sections, $A_m - A'_m$ and $B_m - B'_m$, as depicted in Fig. 1(a). The cross section $B_m - B'_m$ contains the central positions of air hole cylinders while the cross section $A_m - A'_m$ is shifted from the cross section $B_m - B'_m$ by a half periodicity along the y axis. The two cross sections $A_m - A'_m$ and $B_m - B'_m$ are positioned at

$$y_{A,m} = [\sqrt{3}(2m-1)/4]a, \tag{2a}$$

$$y_{B,m} = (\sqrt{3}/2)ma, \tag{2b}$$

where m is an integer. It should be mentioned that selecting the cross section $A_m - A'_m$ allows one to arrange air hole cylinders in the same lattice constant when we consider the interface of two PC media having different radii of air hole cylinders for the two PC media. We calculate the variation of the transverse impedance as a function of wavelength based on Eq. (1) in the case of the TM wave excitation along the y axis. We see that the antireflection PC has different values at the two different cross sections $y_{A,m}$ (blue solid line) and $y_{B,m}$ (green dashed-dotted line) described in Eqs. (2a) and (2b), as shown in Fig. 2(a), where the impedance is normalized with respect to the free space impedance Z_0. The host PC at $y_{A,m}$ has smaller impedance that goes to zero with the decrease of the wavelength in the wavelength range shown in the figure (pink dashed line). To consider an antireflection structure for the host PC in air, the impedance Z_h of the host PC and the impedance Z_{ar} of the antireflection structure need to meet the well-known antireflection condition $Z_{ar}^2 \approx Z_h$, which is discussed in detail in Sec. III. Consequently, the square of the normalized impedance of the antireflection PC at $y_{A,m}$ (blue solid line) is plotted in Fig. 2(b) with the enlarged

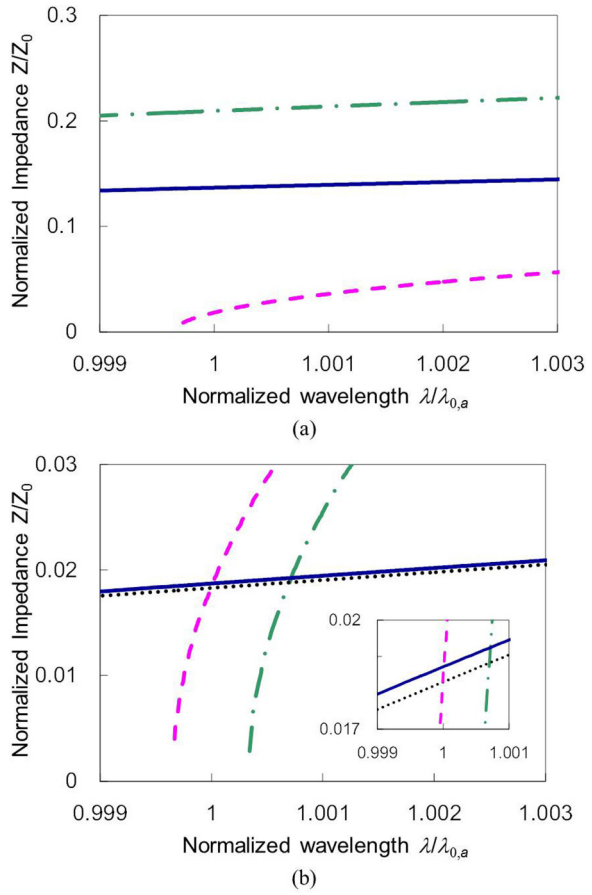

FIG. 2. (Color online) (a) Variation of locally dependent transverse normalized impedances as a function of normalized wavelength in the case of the TM wave propagating along the y axis [blue solid line: $r_{ar} = 269$ mm at $y_{A,m}$ described in Eq. (2a); green dashed-dotted line: $r_{ar} = 269$ mm at $y_{B,m}$ in Eq. (2b); pink dashed line: $r_h = 264$ mm at $y_{A,m}$]. (b) Comparison of the normalized impedance of the host PC (pink dashed line and green dashed-dotted line) and the square of the normalized impedance of the antireflection PC (blue solid line and black dotted line) at $y_{A,m}$. The TM wave propagates parallel to the y axis (blue solid line and pink dashed line) and oblique to the y axis (black dotted line and green dashed-dotted line), corresponding to the case with an incident angle of $\theta_{in} = 3^\circ$ of the TM wave impinged on an antireflection structure.

scale of the vertical axis, and we see that it crosses the host PC normalized impedance (pink dashed line). Moreover, an oblique propagation case is investigated and is plotted in the same figure. The cross point exists at almost the same normalized impedance with a redshift of $0.000\,7\,\lambda_{0,a}$, where angles to the y axis are set at 54° for the host PC and 9.1° for the antireflection PC, respectively. These angles, together with their effective refractive indices, are characterized by the Snell's law and correspond to a 3° angle of the incident wave impinged on an antireflection structure. This indicates that a properly designed antireflection structure may work for some angular ranges of the incident wave with a slight redshift. Note that in such a near-zero effective refractive index case, a small incident angle provides a large refraction angle, obeying Snell's law.

III. ANTIREFLECTION STRUCTURE

Based on the behaviors of the locally dependent impedance as well as the extremely small absolute value of the effective refractive index exhibiting isotropic nature, we present an antireflection structure, as shown in Fig. 3(a). The antireflection structure consists of the PC that has the same lattice constant as the host PC but a different radius of air hole cylinders. This structure allows one to have the cross section at $y_{A,m_0+M_{ar}}$ based on Eq. (2a) for the host PC and the antireflection PC, as well as the feasibility of adjusting the impedance by varying the air-cylinder radius, where M_{ar} is the number of the rows of air hole cylinders of the antireflection PC along the y axis. Selecting another cross section of the antireflection PC at y_{A,m_0} with the air structure enables the same impedance of the antireflection PC at both cross sections; therefore, antireflection behavior can be obtained. In a periodicity of $a = 600$ nm along the x axis around operation wavelength of $\lambda_{0,a}$, the zeroth-order diffraction is the propagating wave, while other higher orders are evanescent waves for reflection and transmission in the diffraction phenomenon at the PC-air interface. We only consider the propagating wave due to the negligibly small effect between the cross sections via evanescent wave coupling.

We introduce an effective medium theory for analytical models while taking into account the local dependence of the transverse impedance in Eq. (1) and utilize a general analysis of the following multilayers. Since the effective refractive indices of the host PC and antireflection PC are isotropic, as evident in Fig. 1(b), here we consider an N-layer structure composed of isotropic media stacked along the y axis for an obliquely incident plane wave with the exp($-i\omega t$) convention. The reflection coefficient at the interface between media j and

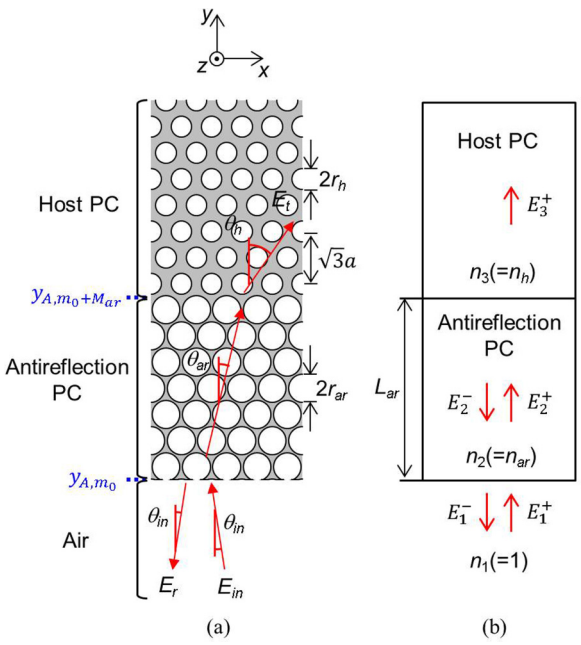

FIG. 3. (Color online) (a) Numerical model of an antireflection PC. The antireflection PC has $M_{ar} = 7$ rows of air hole cylinders along the y axis. (b) Analytical model. The length of the antireflection PC is $L_{ar} = (M_{ar}/2)\sqrt{3}a - \Delta L$, where $\Delta L = 0.03\sqrt{3}a$ is an adjustment amount for fitting analytical results to numerical results.

$j+1$ is expressed with the transverse impedances as

$$r_{j,j+1}(y) = \frac{Z_{j+1}(y) - Z_j(y)}{Z_{j+1}(y) + Z_j(y)}. \quad (3)$$

The electric fields in the Nth layer, E_N^+ and E_N^-, are written in terms of those in the first layer, E_1^+ and E_1^-, as [47]

$$\begin{bmatrix} E_N^+ \\ E_N^- \end{bmatrix} = \begin{bmatrix} A_{1,N} & B_{1,N} \\ C_{1,N} & D_{1,N} \end{bmatrix} \begin{bmatrix} E_1^+ \\ E_1^- \end{bmatrix} = [M_{N-1}][M_{N-2}]\cdots[M_2][M_1]\begin{bmatrix} E_1^+ \\ E_1^- \end{bmatrix}, \quad (4a)$$

where

$$[M_j] = \frac{1}{t_{j+1,j}} \begin{bmatrix} t_{j,j+1}t_{j+1,j} - r_{j,j+1}r_{j+1,j} & r_{j+1,j} \\ -r_{j,j+1} & 1 \end{bmatrix} \times \begin{bmatrix} \exp(i\varphi_j) & 0 \\ 0 & \exp(-i\varphi_j) \end{bmatrix}, \quad (4b)$$

$$\varphi_j = k_j L_j \cos(\theta_j). \quad (4c)$$

The superscripts "+" and "−" denote the propagation direction of the electromagnetic wave along the y axis. $t_{j,j+1}$ is the transmission coefficient at the interface between the media j and $j+1$. k_j and θ_j are the wave number and the propagation angle from the y axis in the jth layer, and L_j is the length of the jth layer. The initial phase factor equals zero, $\varphi_1 = 0$. The reflection coefficient of the total N-layer structure is calculated as $-C_{1,N}/D_{1,N}$. Assuming lossless and reciprocal media in our model, we use $A_{j,j+1} = t_{j,j+1}t_{j+1,j} - r_{j,j+1}r_{j+1,j} = 1$ in Eq. (4b). In the three-layer structure such as our antireflection PC in Fig. 3(b), the reflection coefficient [$N = 3$ in Eqs. (4a)–(4c)] is expressed with a well-known form, $r_{13} = [r_{12} + r_{23}\exp(i2\varphi_2)]/[1 - r_{21}r_{23}\exp(i2\varphi_2)]$. Consequently, our antireflection structure needs to meet the well-known condition $Z_2^2 = Z_1 Z_3$ and $L_2 = [(2u-1)/4]\lambda_2/\cos(\theta_2)$ (u is an integer), based on $r_{13} = 0$. Labels 1, 2, and 3 represent the air media, the antireflection PC, and the host PC, respectively. The minimum length of the antireflection structure is generally a quarter wavelength, which provides the widest bandwidth around the operating wavelength. But the desired effective refractive index cannot be engineered in a quarter-wavelength structure and reflection cannot be suppressed for the near-zero effective refractive index case. Here, instead, the length of the antireflection is set at three-quarters of wavelengths so that the antireflection layer has enough periodicity and possesses the refractive index of Figs. 1(b) and 1(c), which is obtained under the assumption of infinite PCs.

IV. RESULTS

The reflection response of our antireflection structure is numerically and analytically investigated, and the effectiveness of the antireflection behavior and the validity of the analytical model are discussed. The numerical model and its analytical model are shown in Figs. 4(a) and 4(b). The host PC has antireflection PCs at both ends. The interfaces of the antireflection PC with the host PC and with the air structure meet the $A_m - A'_m$ condition in Eq. (2a), and the regions of the antireflection PC and the host PC are defined between each of the $A - A'$ lines. In the numerical model, the host PC and the antireflection PC have the same lattice constant of $a = 600$ nm of periodic air hole cylinders and have radii of $r_h = 264$ nm and $r_{ar} = 269$ nm, as mentioned in Sec. II. The antireflection PC has $M_{ar} = 7$ rows of air hole cylinders along the y axis, as depicted in the schematic illustration of Fig. 3(a), so that the length of the antireflection PC along the y axis is three-quarters of the wavelengths, whereas the host PC has $M_h = 55$ rows of cylinders so that each of the antireflection PCs is separated enough for an accurate evaluation.

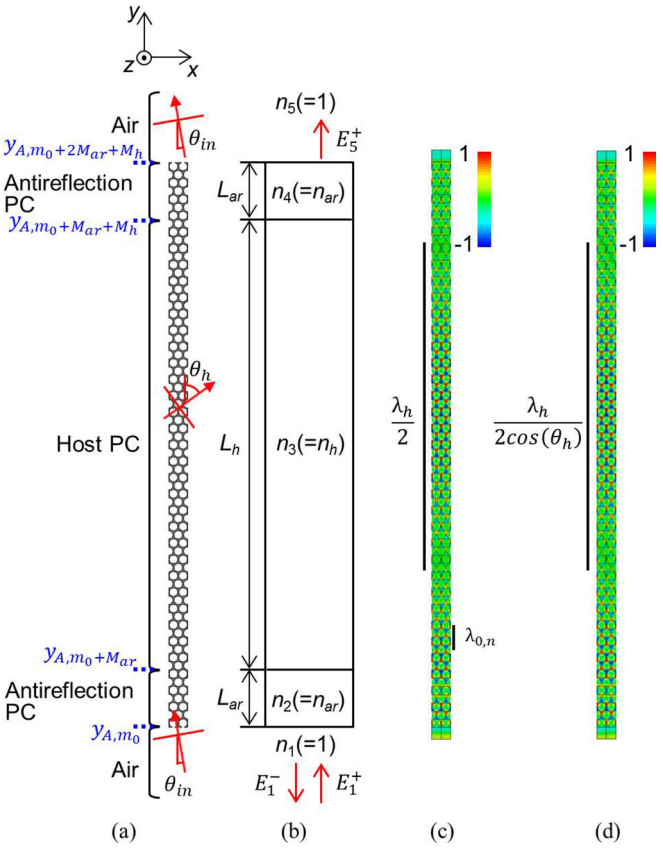

FIG. 4. (Color online) (a) Numerical model of the host PC having the antireflection PCs at both sides. The host and antireflection PCs have $M_h = 55$ rows and $M_{ar} = 7$ rows of air hole cylinders along the y axis. (b) The analytical model has lengths of $L_{ar} = (M_{ar}/2)\sqrt{3}a - \Delta L$ for the antireflection PC and $L_h = (M_h/2)\sqrt{3}a + 2\Delta L$ for the host PC, where $\Delta L = 0.03\sqrt{3}a$ is an adjustment amount for fitting analytical results to numerical results. Snapshots of the electric field distributions are shown in (c) for $\theta_{in} = 0^\circ$ and $\lambda_{0,n} = 1557.1$ nm and in (d) for $\theta_{in} = 3^\circ$ and $1.000\,7\,\lambda_{0,n}$.

The numerical simulation of the reflectance in Fig. 4(a) is performed using the finite-integration-technique-based simulator, CST Microwave Studio [48], at the normal incidence and the oblique incidence of $\theta_{in} = 3^\circ$, and the results as a function of the normalized wavelength are shown in Figs. 5(a) and 5(b), respectively. The wavelength is normalized by $\lambda_{0,n} = 1557.1$ nm for numerical results and by $\lambda_{0,a}$ for analytical results. The discrepancy of $\lambda_{0,n}$ and $\lambda_{0,a}$ is 0.1%. For each incident angle, the reflection of the entire structure is suppressed below −14 dB (blue solid lines, for normal incidence) around $\lambda_n(\lambda_a)$ and $1.000\,7\,\lambda_n(\lambda_a)$ (for the oblique incidence at $\theta_{in} = 3^\circ$). The analytical results of the entire

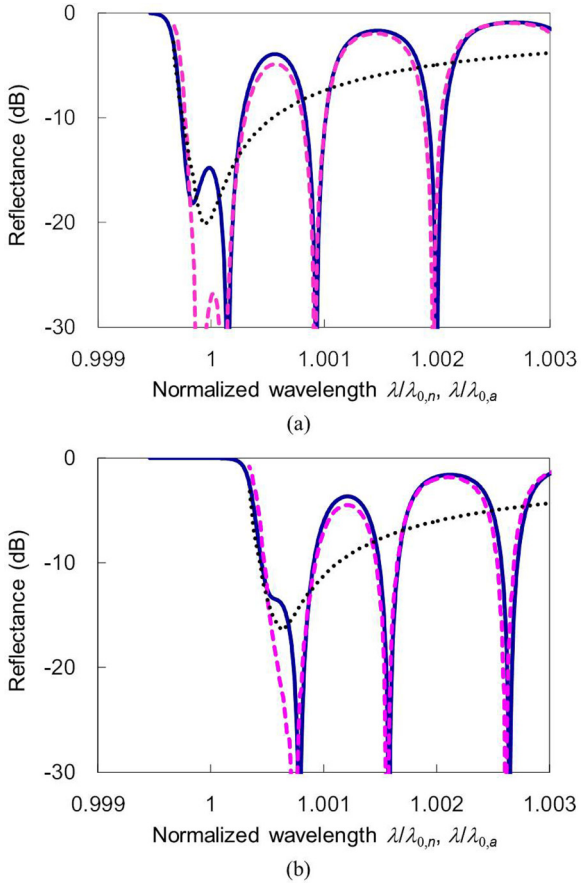

FIG. 5. (Color online) Variation of reflectance as a function of normalized wavelength for incident angles of (a) $\theta_{in} = 0^\circ$ and (b) $\theta_{in} = 3^\circ$ [blue solid lines: numerical results of the entire structure of Fig. 4(a); pink dashed lines: analytical results of the entire structure of Fig. 4(b); black dotted lines: analytical results of the single antireflection structure of Fig. 3(b)].

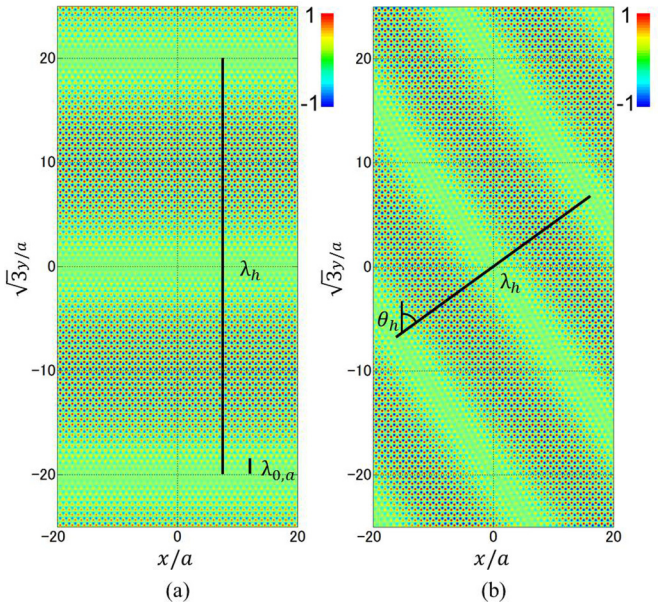

FIG. 6. (Color online) Snapshots of the electric field distributions in the infinite PC (a) at $\theta_h = 0^\circ$ and $\lambda_{0,a}$ and (b) at $\theta_h = 54^\circ$ and $1.000\,7\,\lambda_{0,a}$. These electric field distributions correspond to those of the host PC of the entire PC structure for incident angles of $\theta_{in} = 0^\circ$ [Fig. 4(c)] and 4(b) $\theta_{in} = 3^\circ$ [Fig. 4(d)].

structure (pink dashed lines), which are obtained using Eqs. (4a)–(4c) with the analytical model of Fig. 4(b), agree with the numerical results in the wavelength range of the figure. The reflection level and the periodic dips in Figs. 5(a) and 5(b) relate to the transverse impedance in Eq. (1) [Fig. 2(b)] and the effective refractive index of the host PC [Fig. 1(c)], respectively. We verify that our analytical theory predicts the reflection characteristics accurately. In the analytical results, the lengths of the antireflection PC and the host PC are slightly adjusted to $L_{ar} = (M_{ar}/2)\sqrt{3}a - \Delta L$ (0.9% reduction with $\Delta L = 0.03\sqrt{3}a$) and $L_h = (M_h/2)\sqrt{3}a + 2\Delta L$ for fitting with the numerical results. This adjustment may come from the discrepancy between the *effective* length of the antireflection PC in the numerical model of Fig. 4(a) with the *defined* length in the analytical model of Fig. 4(b). The same lattice constant of air hole cylinders in the host PC and the antireflection PC allows us to *define* the interface [e.g., $y_{A,m}$ in Fig. 1(a)] positioned at the middle of the two cross sections (e.g., $y_{B,m\text{-}1}$ and $y_{B,m}$) containing central positions of the neighboring air hole cylinders across the interface. It is not surprising that the interface is *effectively* shifted by 0.9% of the length of the antireflection PC, since different radii of air hole cylinders in each PC medium provide large changes in effective refractive indices and the electromagnetic fields across the interface. Plotting the analytical response of the intrinsic reflection of the single antireflection structure (black dotted lines) makes clear that the multiple dips are generated by multireflection in the entire structure.

The snapshots of the electric field distributions obtained from the numerical model of Fig. 4(a) are shown in Figs. 4(c) and 4(d) for incident angles of $\theta_{in} = 0^\circ$ and $\theta_{in} = 3^\circ$, respectively. The TM wave propagates through the PC model without reflection in both cases. Due to the constraint in the computational volume of our numerical simulations and the display function of the simulator, we only present the simulations in the area with width of $2a$ in the x axis.

An extremely long wavelength and large refraction angle in the host PC are visualized with the electric field distributions of the infinite PC obtained by the plane-wave expansion method in [see Figs. 6(a) and 6(b)], since we have confirmed the agreement between the numerical and analytical results in the reflection response. The propagation angles to the y axis and the operating wavelengths are the same as for the case of the analytical structure that are $\theta_h = 0^\circ$ and λ_a [Fig. 6(a)] and $\theta_h = 54^\circ$ and $1.000\,7\ \lambda_a$ [Fig. 6(b)], respectively. In Table I, we summarize the antireflection behavior for the two incident-angle scenarios. We clearly verify that the antireflection condition is almost met, $Z_{ar}^2 \approx Z_h$ and $L_{ar} \approx (3/4)\,\lambda_{ar}/\cos(\theta_{ar})$, even for small absolute values of effective refractive indices for the normal and oblique incidence angles.

We note from the analytical results that the reflection of the entire structure (five layers in Table I) is smaller than that of the intrinsic reflection (three layers in Table I). This indicates that the reflection response includes a fraction generated by

TABLE I. Summary of the antireflection behavior. Parameter values of the host PC and the antireflection PC are calculated in the infinite PC model [Fig. 1(a)]. Reflectances are obtained by the analytical models of the three layers [Fig. 3(b)] and the five layers [Fig. 4(b)]. Values in parentheses are obtained from the numerical models of the three layers [Fig. 3(a)] and the five layers [Fig. 4(a)].

		Host PC					Antireflection PC					Reflectance	
θ_{in}	λ/λ_a	n_h	λ_h	θ_h	Z_h/Z_0	$\frac{\lambda_h}{\cos(\theta_h)}$	n_{ar}	λ_{ar}	θ_{ar}	Z_{ar}/Z_0	$\frac{(3/4)\lambda_{ar}}{\cos(\theta_{ar})}$	Three layers	Five layers
0º	1	−0.0374	$40\sqrt{3}a$	0º	0.0185	$40\sqrt{3}a$	−0.325	$4.6\sqrt{3}a$	0º	0.137	$3.45\sqrt{3}a$	−19.5 dB	–27.1 dB (–14.9 dB)
3º	1.0007	−0.0647	$23.1\sqrt{3}a$	54º	0.0188	$39.4\sqrt{3}a$	−0.331	$4.52\sqrt{3}a$	9.1º	0.137	$3.44\sqrt{3}a$	−15.7 dB	–27.3 dB (–16.6 dB)

multiple reflections in the entire structure. In other words, the reflection level of the entire structure is varied a little from the intrinsic reflection level when the length of the host PC is changed. Table I also shows that the wavelength in the host PC along the y direction, $\lambda_h/\cos(\theta_h)$, has nearly the same values for the two incident-angle cases. Thus the two electric field distributions of Figs. 4(c) and 4(d) seem to be nearly the same profiles.

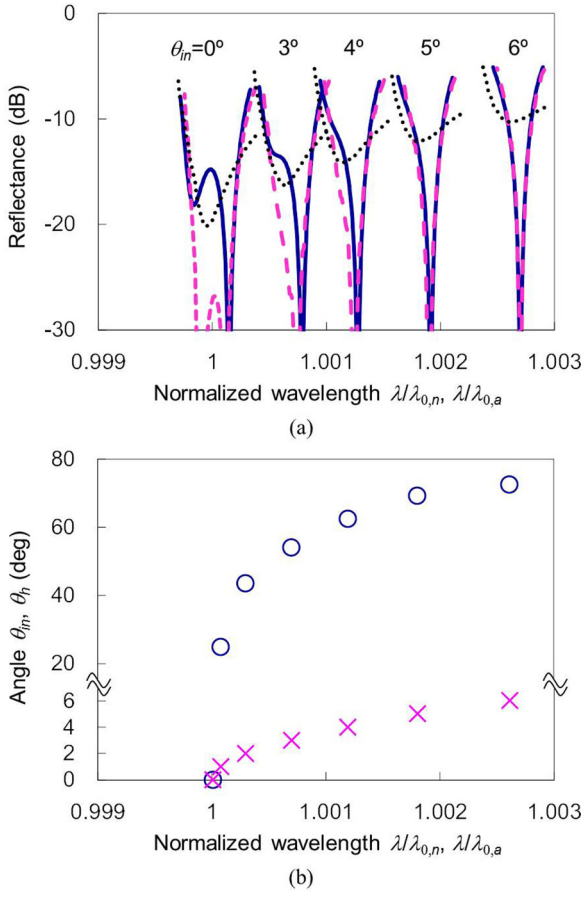

FIG. 7. (Color online) (a) Variation of reflectance as a function of normalized wavelength for incident angles of $\theta_{in} = 0^\circ$, 3º, 4º, 5º, and 6º. Reflectance around the reflection-suppressed wavelength is presented for each of the incidence angles. The reflection-suppressed wavelength is redshifted with increasing the incident angle [blue solid lines: numerical results of the entire structure of Fig. 4(a); pink dashed lines: analytical results of the entire structure of Fig. 4(b); black dotted lines: analytical results of the single antireflection structure of Fig. 3(b)]. (b) Variation of refraction angles (circles) as a function of normalized wavelength for incident angles (crosses) of $\theta_{in} = 0^\circ - 6^\circ$ with a step of 1º.

In order to better understand the angular and frequency dependence of the antireflection behavior, we vary the incident angle from 0º to 6º and plot the reflection characteristics (0º, 3º, 4º, 5º, and 6º for clarity) in Fig. 7(a) and refraction angles (with a step of 1º) obtained by Snell's law in Fig. 7(b). We see that the reflection of the single antireflection structure [three layers in Fig. 3(b)] stays below −10 dB (black dotted lines) in the incident-angle range of 0º–6º with the redshift of the reflection-suppressed wavelength. In addition, we see the agreement between the numerical (blue solid lines) and analytical (pink dashed lines) results for the entire structure [five layers in Figs. 4(a) and 4(b)]. The refraction angle is varied widely from 0º to 72º (circles) due to the near-zero effective refractive index of the host medium.

V. CONCLUSIONS

We have presented an antireflection PC for the host PC having near-zero effective refractive index. The antireflection PC has the same lattice constant of air hole cylinders as that of the host PC, but a different radius of air hole cylinders. This enables us to have the same impedance at interfaces of the antireflection PC with the host PC and with the air structure at properly selected cross sections as well as the flexibility of impedance control by varying the radius of the air hole cylinders. The length of the antireflection PC is three-quarter wavelengths (instead of a quarter wavelength) in order to engineer the desired effective refractive index with enough periodicity of the air hole cylinders. Numerical results have shown that our structure sufficiently suppresses the reflection at normal incidence and within a range of oblique incidence with slight redshift.

We have developed an analytic theory by introducing an effective medium theory. Owing to the isotropic nature of the effective refractive indices near the second band edge in the dispersion, the antireflection PC and the host PC are modeled as isotropic and homogeneous layers. In addition, the local dependence of the impedance at each interface is taken into account. The analytic theory has captured the antireflection behavior obtained by numerical simulations.

Our antireflection PC is designed based on a general antireflection theory by considering the features of near-zero effective refractive index and is different from other antireflection structures determined by geometrical optimization. Therefore, our results point to an important design guideline of antireflections for the effective refractive indices of near-zero PCs.

[1] N. Engheta, Science **340**, 286 (2013).
[2] M. G. Silveirinha and N. Engheta, Phys. Rev. Lett. **97**, 157403 (2006).
[3] M. G. Silveirinha and N. Engheta, Phys. Rev. B **75**, 075119 (2007).
[4] M. G. Silveirinha and N. Engheta, Phys. Rev. B **76**, 245109 (2007).
[5] A. Alu, M. G. Silveirinha, and N. Engheta, Phys. Rev. E **78**, 016604 (2008).
[6] A. Alu and N. Engheta, Phys. Rev. B **78**, 035440 (2008).
[7] A. Alu and N. Engheta, Phys. Rev. B **78**, 045102 (2008).
[8] J. Hao, W. Yan, and M. Qiu, Appl. Phys. Lett. **96**, 101109 (2010).
[9] F. J. Rodriguez-Fortuno, A. Vakil, and N. Engheta, Phys. Rev. Lett. **112**, 033902 (2014).
[10] Mario G. Silveirinha and N. Engheta, Phys. Rev. Lett. **102**, 103902 (2009).
[11] C. Argyropoulos, P.-Y. Chen, G. D'Aguanno, N. Engheta, and A. Alu, Phys. Rev. B **85**, 045129 (2012).
[12] A. Alu and N. Engheta, Phys. Rev. Lett. **103**, 143902 (2009).
[13] A. Alu and N. Engheta, Opt. Express **15**, 13773 (2007).
[14] M. G. Silveirnha, A. Alu, J. Li, and N. Engheta, J. Appl. Phys. **103**, 064305 (2008).
[15] A. Alu and N. Engheta, IEEE Trans. Antennas Propag. **58**, 328 (2010).
[16] A. Alu, M. G. Silveirinha, A. Salandrino, and N. Engheta, Phys. Rev. B **75**, 155410 (2007).
[17] A. R. Davoyan, A. M. Mahmoud, and N. Engheta, Opt. Express **21**, 3279 (2013).
[18] S. Vassant, A. Archambault, F. Marquier, F. Pardo, U. Gennser, A. Cavanna, J. L. Pelouard, and J. J. Greffet, Phys. Rev. Lett. **109**, 237401 (2012).
[19] S. Molesky, C. J. Dewalt, and Z. Jacob, Opt. Express **21**, A96 (2013).
[20] B. Edwards, A. Alu, M. E. Young, M. G. Silveirinha, and N. Engheta, Phys. Rev. Lett. **100**, 033903 (2008).
[21] B. Edwards, A. Alu, M. G. Silveirnha, and N. Engheta, J. Appl. Phys. **105**, 044905 (2009).
[22] B. Edwards and N. Engheta, Phys. Rev. Lett. **108**, 193902 (2012).
[23] D. A. Powell, A. Alu, B. Edwards, A. Vakil, Y. S. Kivshar, and N. Engheta, Phys. Rev. B **79**, 245135 (2009).
[24] R. J. Pollard, A. Murphy, W. R. Hendren, P. R. Evans, R. Atkinson, G. A. Wurtz, A. V. Zayats, and V. A. Podolskiy, Phys. Rev. Lett. **102**, 127405 (2009).
[25] D. C. Adams, S. Inampudi, T. Ribaudo, D. Slocum, S. Vangala, N. A. Kuhta, W. D. Goodhue, V. A. Podolskiy, and D. Wasserman, Phys. Rev. Lett. **107**, 133901 (2011).
[26] Ernst Jan R. Vesseur, T. Coenen, H. Caglayan, N. Engheta, and A. Polman, Phys. Rev. Lett. **110**, 013902 (2013).
[27] R. Maas, J. Parsons, N. Engheta, and A. Polman, Nat. Photonics **7**, 907 (2013).
[28] M. Notomi, Phys. Rev. B **62**, 10696 (2000).
[29] E. Cubukcu, K. Aydin, E. Ozbay, S. Foteinopoulou, and C. M. Soukoulis, Nature (London) **423**, 604 (2003).
[30] X. Huang, Y. Lai, Z. H. Hang, H. Zheng, and C. T. Chan, Nat. Mater. **10**, 582 (2011).
[31] L. Zhou, Z. Song, X. Huang, and C. T. Chan, Nanophotonics **1**, 181 (2012).
[32] P. Moitra, Y. Yang, Z. Anderson, I. I. Kravchenko, D. P. Briggs, and J. Valentine, Nat. Photonics **7**, 791 (2013).
[33] T. Decoopman, G. Tayeb, S. Enoch, D. Maystre, and B. Gralak, Phys. Rev. Lett. **97**, 073905 (2006).
[34] Z. Lu and D. W. Prather, Opt. Express **15**, 8340 (2007).
[35] W. Smigaj and B. Gralak, Phys. Rev. B **77**, 235445 (2008).
[36] W. Smigaj, B. Gralak, R. Pierre, and G. Tayeb, Opt. Lett. **34**, 3532 (2009).
[37] G. Scherrer, M. Hofman, W. Smigaj, B. Gralak, X. Melique, O. Vanbesien, D. Lippens, C. Dumas, B. Cluzel, and F. de Fornel, Appl. Phys. Lett. **97**, 071119 (2010).
[38] W. Smigaj and B. Gralak, Phys. Rev. B **85**, 035114 (2012).
[39] J. Witzens, M. Hochberg, T. Baehr-Jones, and A. Scherer, Phys. Rev. E **69**, 046609 (2004).
[40] F. J. Lawrence, L. C. Botten, K. B. Dossou, and C. M. de Sterke, Appl. Phys. Lett. **93**, 121114 (2008).
[41] F. J. Lawrence, L. C. Botten, K. B. Dossou, C. M. de Sterke, and R. C. McPhedran, Phys. Rev. A **80**, 023826 (2009).
[42] T. T. Kim, S. G. Lee, M. W. Kim, H. Y. Park, and J. E. Kim, Appl. Phys. Lett. **95**, 011119 (2009).
[43] B. Momeni and A. Adibi, Appl. Phys. Lett. **87**, 171104 (2005).
[44] T. Baba, T. Matsumoto, and M. Echizen, Opt. Express **12**, 4608 (2004).
[45] K. M. Ho, C. T. Chan, and C. M. Soukoulis, Phys. Rev. Lett. **65**, 3152 (1990).
[46] R. W. Ziolkowski and E. Heyman, Phys. Rev. E **64**, 056625 (2001).
[47] B. E. A. Saleh and M. C. Teich, *Fundamentals of Photonics*, 2nd ed. (John Wiley & Sons, Hoboken, NJ, 2007).
[48] CST Microwave Studio 2013, http://www.cst.com